



Material coherence and life cycle of a wildfire-generated stratospheric vortex

Fernando Andrade-Canto¹ and Francisco J. Beron-Vera²

¹Departamento de Observación y Estudio de la Tierra, la Atmósfera y el Océano, El Colegio de la Frontera Sur, Chetumal, Quintana Roo, Mexico

²Department of Atmospheric Sciences, Rosenstiel School of Marine, Atmospheric & Earth Science, University of Miami, Miami, Florida, USA

Correspondence: Fernando Andrade-Canto (fernando.andrade@ecosur.mx) and Francisco J. Beron-Vera (fberon@miami.edu)

Abstract. Pyro-cumulonimbus convection associated with extreme wildfires can generate long-lived vortical structures in the stratosphere. These structures have been described as coherent, yet a rigorous material characterization has remained lacking. Here we provide such a characterization by applying geodesic vortex detection to reanalysis winds during the 2019–2020 Australian bushfires.

5 We identify a coherent Lagrangian vortex, dubbed *Koobor*, whose boundary is given by materially coherent loops exhibiting nearly uniform stretching and strong resistance to filamentation over finite time intervals of up to 40 days. The detected vortex extends across multiple isentropic levels, revealing a vertically organized evolution with delayed onset and reduced persistence at higher levels.

10 Taken together across isentropic levels, the reconstructed life cycle indicates that *Koobor* maintained quasi-material coherence for nearly 60 days from its first detection, through a sequence of overlapping materially coherent boundaries rather than a single boundary advected over the entire period.

Our results establish a material framework for wildfire-induced stratospheric vortices and provide a dynamically consistent description of their life cycle, from formation to decay.

1 Introduction

15 Since the 2010s, a growing body of work (Fromm et al., 2010; de Laat et al., 2012; Yu et al., 2019; Peterson et al., 2018; Khaykin et al., 2020) has documented that large summer wildfires in mid-latitude forests can generate pyro-cumulonimbus (pyroCb) clouds capable of injecting combustion products into the lower stratosphere. These products, including organic and black carbon, smoke aerosols, and carbon monoxide, can persist for several months and be transported over intercontinental distances, reaching even tropical latitudes. Absorption of solar radiation by black carbon leads to diabatic heating, which
20 enhances plume buoyancy and can loft the injected material several kilometers higher into the stratosphere. This self-lofting mechanism promotes vertical growth and prolonged residence times, amplifying the radiative impact of the plume to levels comparable to those of moderate volcanic eruptions.



The 2019–2020 Australian wildfires constitute an extreme realization of this phenomenon (Khaykin et al., 2020; Kablick et al., 2020; Allen et al., 2020). Several stratospheric smoke plumes formed long-lived anticyclonic vortices with lifetimes on the order of 1–3 months. The most prominent of these, referred to as *Koobor*, ascended to altitudes approaching 35 km, unprecedented for wildfire-driven injections and comparable to those observed following the *Pinatubo* eruption. Aerosol-induced heating has been identified as a key mechanism sustaining these structures (Khaykin et al., 2020), enabling them to maintain vertical integrity while confining smoke and delaying dispersion.

Despite these advances, the dynamical nature and material coherence of such vortices remain only partially characterized. Previous studies have relied primarily on Eulerian diagnostics. For example, Khaykin et al. (2020) examined relative vorticity, while Lestrelin et al. (2021) considered potential vorticity and ozone anomalies relative to zonal means. More recently, Curbelo and Rypina (2023) applied nonlinear dynamical systems tools to heuristically identify attracting and repelling material structures corresponding to hyperbolic Lagrangian coherent structures (LCS) (Haller, 2023). However, the smoke-containing vortices observed in pyroCb events are not primarily organized by hyperbolic transport barriers, but instead exhibit a coherent rotating core consistent with an *elliptic* LCS.

In this work, we adopt a complementary perspective by focusing on elliptic LCS, which capture materially coherent vortices. Specifically, we apply *geodesic vortex detection* (Haller and Beron-Vera, 2013, 2014; Andrade-Canto et al., 2025), a nonlinear dynamical systems framework that identifies vortex boundaries as closed material curves experiencing near-uniform stretching. Such boundaries resist the filamentation that typically affects material loops in strongly deforming flows, thereby providing an objective definition of vortex coherence over a finite time interval.

We apply this framework to reanalysis wind fields to investigate the structure and evolution of the *Koobor* plume. Despite known limitations of reanalysis data in representing small-scale and rapidly evolving features, the results reveal a coherent Lagrangian vortex with a vertical extent of approximately 6 km, spanning a substantial portion of the lower and middle stratosphere. The full life cycle of this structure—from formation to dissipation—is reconstructed using a Lagrangian tracking methodology introduced in Andrade-Canto et al. (2020) and previously applied in oceanographic (Andrade-Canto and Beron-Vera, 2022) and atmospheric (Andrade-Canto et al., 2025) contexts.

While a detailed assessment of reanalysis fidelity is beyond the scope of this study, our findings are consistent with the view that assimilated temperature fields can constrain the large-scale, balanced dynamics governing stratospheric motion (McIntyre, 2015). The results therefore support the use of such datasets for investigating the material organization and transport properties of long-lived stratospheric smoke vortices.

2 Methodology

2.1 Lagrangian framework and vortex definition

We analyze atmospheric motion on isentropic surfaces within a nonlinear dynamical systems framework. On each isentropic level, the flow is modeled as a two-dimensional, time-dependent velocity field $\mathbf{u}(\mathbf{x}, t)$ defined on an open domain $U \subset \mathbb{R}^2$,



55 where \mathbf{x} denotes horizontal position. The evolution of air parcels is governed by

$$\dot{\mathbf{x}} = \mathbf{u}(\mathbf{x}, t), \quad \mathbf{x}(t_0) = \mathbf{x}_0, \quad (1)$$

with associated flow map $\mathbf{F}_{t_0}^t : U \rightarrow U$ mapping initial to advected positions.

Within this framework, we seek materially coherent vortices, i.e., regions enclosed by material curves that resist the strong stretching and filamentation typical of unsteady flows. We adopt the geodesic vortex detection framework (Haller and Beron-
60 Vera, 2013, 2014; Andrade-Canto et al., 2025), which provides an objective (observer-independent) definition of vortex boundaries as closed material loops that undergo uniform stretching, i.e., each subset of the loop is stretched by the same factor over the interval $[t_0, t_0 + T]$.

This notion arises from a variational characterization of material coherence: vortex boundaries are closed material curves that undergo uniform stretching over $[t_0, t_0 + T]$, thereby avoiding the differential stretching that leads to filamentation. These
65 curves can be interpreted as null-geodesics of a Lorentzian metric induced by a generalized Green–Lagrange strain tensor constructed from the Cauchy–Green tensor.

In practice, they are computed as limit cycles of a parameterized line field derived from the Cauchy–Green tensor associated with the flow map $\mathbf{F}_{t_0}^t$, with the outermost closed loop defining the vortex boundary. A concise summary of the underlying variational principle and its numerical realization is provided in Appendix A.

70 2.2 Life-cycle characterization

To characterize the temporal evolution of vortices, we employ the extended detection framework introduced in Andrade-Canto et al. (2020), which enables the identification of formation and dissipation times through a systematic exploration of the parameter space (t_0, T) .

For each initial time t_0 within a prescribed window, geodesic vortex detection is applied over increasing time intervals $T > 0$
75 until no coherent vortex boundary can be identified. This defines a maximal coherence time $T_{\text{exp}}(t_0)$, representing the longest interval over which material coherence persists for that initialization. Repeating this procedure over a range of t_0 yields a function $T_{\text{exp}}(t_0)$ that typically exhibits a wedge-like structure, with coherence degrading away from an optimal initialization time.

The vortex birth time t_{birth} is identified as the time at which T_{exp} attains its maximum, while the death time t_{death} is defined
80 as the end of the corresponding maximal coherence interval. To refine these estimates, the procedure is also applied in backward time, as described in Appendix B.

2.3 Two-dimensional approximation and coherence horizon

The above analysis relies on the approximation of the flow as two-dimensional on isentropic surfaces. This approximation is valid only over finite time intervals due to diabatic effects and cross-isentropic transport, which induce vertical motion and
85 eventually invalidate the two-dimensional description (Haynes, 2005).



This limitation is particularly relevant in the present context, as pyroCb-generated smoke plumes undergo buoyancy-driven ascent and therefore exhibit intrinsically three-dimensional motion. The coherent structures identified here should thus be interpreted as horizontal manifestations of this evolving three-dimensional flow, rather than as material surfaces that remain confined to a single isentropic level. In contrast to approaches that explicitly incorporate buoyancy and vertical transport in a fully three-dimensional framework, such as Curbelo and Rypina (2023), the present analysis focuses on finite-time material coherence within individual isentropic layers.

We therefore introduce a coherence horizon τ and restrict the analysis to time intervals satisfying $T \leq \tau$, following Andrade-Canto et al. (2025). This constraint limits the admissible coherence times and leads to a truncation of the ideal wedge structure of $T_{\text{exp}}(t_0)$ at $T \approx \tau$. In this regime, the latest initialization time for which coherence persists up to τ provides an estimate of the vortex death time, while the birth time is obtained by backward-time analysis from this estimate.

Because the total lifetime inferred in this way may exceed τ , the detected vortices are interpreted as quasi-coherent structures, maintaining material coherence only over finite overlapping intervals of duration τ . This perspective is consistent with a vertically evolving plume whose coherent core is intermittently captured across successive isentropic levels.

2.4 Data

We analyze isentropic wind fields from the ECMWF ERA5 reanalysis (Hersbach et al., 2020), which combines observational data with short-term forecasts through data assimilation. The dataset covers the Southern Hemisphere during 2019–2020, with a horizontal resolution of approximately 31 km and a temporal resolution of 6 hours. The analysis is performed on the 550, 590, 630, 690, 770, 850, and 964 K isentropic levels, allowing us to assess the vertical structure and persistence of coherent vortices across the lower and middle stratosphere.

2.5 Computational implementation

Geodesic vortex detection and trajectory computations are carried out using the CoherentStructures.jl package, adapted to spherical geometry Andrade-Canto et al. (2025). The computation proceeds by constructing the flow map from trajectory integration, evaluating the associated Cauchy–Green strain tensor, extracting limit cycles of the resulting line field, and selecting the outermost closed loop as the vortex boundary. Implementation details, including interpolation, grid resolution, and numerical integration schemes, are provided in Appendix A.

3 Results

We apply the nonlinear dynamical systems framework to ERA5 isentropic winds to characterize the spatial structure and temporal development of the *Koobor* smoke plume Khaykin et al. (2020). The analysis follows the isentropic configuration described above, with initial times t_0 sampled every 5 days (3 days at the highest level due to shorter coherence horizons).

For each level, we identify the vortex boundary achieving the largest coherence time in forward or backward time, capped at $\tau = 40$ days to remain consistent with the quasi-two-dimensional approximation on isentropic surfaces (Haynes, 2005).



120 Isentropic surfaces in the lower and middle stratosphere during austral summer and early autumn are approximately surfaces of nearly constant altitude, owing to strong stratification and weak diabatic forcing on synoptic time scales (Holton, 1979). Consequently, the levels considered here (590–850 K) correspond roughly to altitudes between 22 and 30 km (Table 1), allowing a direct interpretation of the detected vertical structure in terms of geometric height.

The large-scale evolution of the smoke plume provides the physical context for the detected vortex. Following the Australian wildfires, the plume is advected eastward across the Southern Hemisphere and reaches the South American sector near Patagonia. During this stage, radiative heating of absorbing aerosols induces diabatic ascent, lifting the plume into the stratosphere where rotational organization emerges. Once formed, the *Koobor* vortex exhibits a westward drift consistent with the background stratospheric circulation at these latitudes Holton (1979).

130 Figure 1 illustrates the methodology on the 690 K surface, where material coherence is strongest. The vortex boundary forms between Patagonia and the South Pole and follows a coherent, approximately circular trajectory across the Southern Hemisphere before dissipating near South Africa. The coherence-time ramps display the expected truncated wedge structure, from which we infer a formation date of 27 January 2020 and a decay date of 7 March 2020. The boundary detected at 27 January 2020 is then advected forward in time until the decay date. The resulting lifetime of approximately 40 days identifies this level as the dynamically dominant core of the vortex.

Extending this analysis across all levels (Fig. 2) reveals a vertically organized and temporally coherent structure. The coherence-time fields exhibit consistent truncated-wedge signatures, indicating robust identification of finite-time material coherence. No coherent boundary is detected at 550 or 964 K, suggesting that the vortex is vertically confined.

135 In contrast with Fig. 1, the boundaries shown here are not obtained by advecting a single initial curve. Instead, at each level they result from the life-cycle analysis, which identifies, for each initialization time, a vortex boundary that remains materially coherent over a finite time interval capped at 40 days. Each such boundary is a material curve exhibiting nearly uniform stretching over its corresponding interval. The displayed sequence therefore does not represent the evolution of a single material surface, but rather a collection of material curves defined over overlapping time windows. In this sense, the vortex is depicted as a quasi-material entity, whose coherence is sustained locally in time but not by a single globally advected boundary.

145 A clear upward progression is observed. The vortex first appears at 590 K on 7 January 2020, followed by 630 K on 22 January and 690 K on 27 January. Higher levels (770 and 850 K) emerge only in early February, indicating a delayed upward development. This lag is consistent with diabatically driven ascent of the smoke plume prior to the establishment of coherent rotational dynamics.

The decay phase exhibits the opposite behavior. Coherence is lost first at higher levels, with lifetimes of 12 days at 850 K and 15 days at 770 K, while lower levels persist longer (25–30 days). The longest lifetime occurs at 690 K (40 days), indicating a vertically localized maximum in material coherence. The horizontal trajectory shown in Fig. 2 further demonstrates that the vortex maintains large-scale coherence while advecting across the hemisphere.

150 Table 1 summarizes the life-cycle properties across levels. The correspondence between isentropic surfaces and geometric height indicates that the vortex core is centered near 26 km (690 K), with decreasing coherence both above and below this



Level	Birth	Death	Lifetime	Radius
590 K (22 km)	2020-01-07	2020-02-06	30 d	104 km
630 K (24 km)	2020-01-22	2020-02-16	25 d	106 km
690 K (26 km)	2020-01-27	2020-03-07	40 d	111 km
770 K (28 km)	2020-02-06	2020-02-21	15 d	118 km
850 K (30 km)	2020-02-07	2020-02-19	12 d	138 km

Table 1. Life-cycle properties of *Koobor*. Approximate altitude corresponding to each isentropic level is indicated in parentheses.

level. The reported radii correspond to equivalent circles of the detected vortex boundaries at the times when the coherence horizon is maximal. Across levels, the earliest birth and latest decay dates do not coincide, but together indicate that *Koobor* persists as a coherent Lagrangian vortex over a period approaching 60 days.

155 Figure 3 synthesizes the evolution across all levels. Early in the life cycle, only the lowest level (590 K) exhibits a coherent boundary. Intermediate levels (630 and 690 K) subsequently emerge and dominate the dynamics, while higher levels (770 and 850 K) appear transiently near the midpoint of the life cycle. The vortex reaches its maximum vertical extent around early February and then decays from the top downward, consistent with enhanced deformation and mixing in the upper stratosphere.

160 The translucent tubes connect vortex boundaries detected at different isentropic levels on the same date and therefore represent instantaneous vertical envelopes of the structure. As in Fig. 2, these boundaries are not obtained by advecting a single material curve, but arise from the life-cycle analysis in which coherence is evaluated over finite time intervals capped at 40 days. The tubes thus provide a visual synthesis of quasi-material coherence across levels, capturing the vertical organization of the vortex at discrete times without implying the existence of a single advected material surface.

165 Overall, the results reveal a coherent Lagrangian vortex that forms through the upward organization of a diabatically ascending plume, reaches peak coherence at intermediate levels, and decays while maintaining a well-defined large-scale trajectory. This vertically structured evolution is consistent with a dynamically robust core embedded within a transient three-dimensional plume.

170 The variability in coherence times across isentropic levels reflects differences in the persistence of material coherence. Vortices identified at higher potential temperatures (e.g., 770–850 K), corresponding to higher isentropic surfaces, exhibit shorter coherence times, while intermediate levels (notably 690 K) sustain coherence over longer intervals. This indicates that the ability of the flow to support materially coherent vortices varies significantly with altitude, with a pronounced maximum at intermediate levels.

4 Conclusions

175 We have analyzed the evolution of the stratospheric smoke vortex *Koobor*, generated by the 2019–2020 Australian wildfires, using a nonlinear dynamical systems framework based on geodesic vortex detection and life-cycle reconstruction. This ap-



proach enables an objective identification of materially coherent vortex boundaries together with a consistent definition of vortex birth, persistence, and decay.

The results reveal a coherent vortex with a well-defined finite-time life cycle. The structure first appears at lower isentropic levels (590 K) and subsequently develops upward, reaching higher levels (up to 850 K) with a systematic delay. Maximum coherence is attained at an intermediate level (690 K), where the vortex persists for approximately 40 days, while coherence at higher levels is both delayed in onset and shorter-lived. No coherent boundary is detected at 550 and 964 K, indicating that the structure remains vertically confined.

The combined forward- and backward-time analysis shows that the vortex undergoes a characteristic evolution consisting of upward development, peak coherence at intermediate levels, and decay from the top downward. This organization is consistent with a diabatically ascending smoke plume that forms a dynamically robust core in the lower and middle stratosphere, with reduced coherence both above and below. Throughout its evolution, the vortex remains materially coherent while undergoing large-scale advection across the Southern Hemisphere.

Taken together across isentropic levels, the life-cycle reconstruction indicates that *Koobor* maintained quasi-material coherence for nearly 60 days from its first detection. This extended duration reflects the persistence of materially coherent boundaries over overlapping finite-time intervals, rather than the advection of a single boundary over the entire period.

Because the analysis is restricted to finite coherence horizons imposed by the two-dimensional approximation on isentropic surfaces, the detected structures are interpreted as quasi-coherent vortices. Nevertheless, the consistency of the coherence-time diagnostics across levels indicates that the inferred life cycle captures a robust and physically meaningful evolution.

These results show that geodesic vortex detection, combined with life-cycle analysis, provides a framework for quantifying the material coherence and temporal development of wildfire-generated stratospheric vortices. Despite the known limitations of reanalysis winds, the detected structure exhibits a high degree of internal consistency, indicating that the dominant balanced dynamics of the flow are adequately represented.

These findings highlight the relevance of a nonlinear dynamical systems perspective for the study of pyroCb-generated vortices and provide a basis for future work on their three-dimensional structure, vertical coupling, and radiative–dynamical interactions.

Appendix A: Geodesic vortex detection, life-cycle identification, and numerical implementation

A1 Geodesic vortex detection

We briefly summarize the geodesic framework used to identify materially coherent vortices. For full details, see Haller and Beron-Vera (2013, 2014); Haller (2015, 2023); Andrade-Canto et al. (2025).

Let $\mathbf{F}_{t_0}^t$ denote the flow map associated with the velocity field $\mathbf{u}(\mathbf{x}, t)$. The deformation induced by the flow over $[t_0, t_0 + T]$ is quantified by the (right) Cauchy–Green strain tensor

$$C_{t_0}^{t_0+T}(\mathbf{x}_0) = \nabla \mathbf{F}_{t_0}^{t_0+T}(\mathbf{x}_0)^\top \nabla \mathbf{F}_{t_0}^{t_0+T}(\mathbf{x}_0). \quad (\text{A.1})$$



This symmetric, positive-definite tensor admits eigenvalues and orthonormal eigenvectors $0 < \lambda_1(\mathbf{x}_0) \leq \lambda_2(\mathbf{x}_0)$ with corresponding eigenvectors $\mathbf{v}_1(\mathbf{x}_0)$ and $\mathbf{v}_2(\mathbf{x}_0)$.

210 Material vortex boundaries are defined as closed curves that exhibit uniform stretching over $[t_0, t_0 + T]$. Such curves arise as stationary curves of an averaged stretching functional and are characterized as limit cycles of the line field

$$\mathbf{r}'(s) = \mathbf{I}_p^\pm(\mathbf{r}) := \sqrt{\frac{\lambda_2(\mathbf{r}) - p^2}{\lambda_2(\mathbf{r}) - \lambda_1(\mathbf{r})}} \mathbf{v}_1(\mathbf{r}) \pm \sqrt{\frac{p^2 - \lambda_1(\mathbf{r})}{\lambda_2(\mathbf{r}) - \lambda_1(\mathbf{r})}} \mathbf{v}_2(\mathbf{r}), \quad (\text{A.2})$$

for values of p satisfying $\lambda_1(\mathbf{r}) < p^2 < \lambda_2(\mathbf{r})$.

215 Closed orbits of (A.2) form nested families of non-intersecting loops. Each closed orbit is a limit cycle of either the \mathbf{I}_p^+ or the \mathbf{I}_p^- line field, and therefore belongs to a single branch of the field. The existence of such closed orbits is not generic but is guaranteed in regions where the topology of the line field supports limit cycles, as characterized by index theory for planar line fields (Karrasch et al., 2014). In particular, closed orbits arise in neighborhoods of appropriate singularity configurations of the line field, which act as organizing centers for coherent vortex boundaries.

220 Among the resulting family of nested loops, the outermost closed orbit defines the boundary of a coherent Lagrangian vortex. These loops can equivalently be interpreted as null-geodesics of a generalized Green–Lagrangian tensor field. This interpretation is particularly transparent in the incompressible case: since enclosed area is preserved, a loop that stretches uniformly cannot develop the strong differential stretching responsible for filamentation. In the special case $p = 1$, the loop also preserves arclength, so that neither its length nor its enclosed area changes to leading order, further reinforcing resistance to filamentation.

225 An extension of this framework to flows on curved manifolds is developed in Andrade-Canto et al. (2025).

A2 Life-cycle identification

We summarize the procedure used to identify vortex birth and death times following Andrade-Canto et al. (2020), with additional details given here for completeness. The method systematically explores the two-parameter space (t_0, T) by repeatedly applying geodesic vortex detection over varying initial times and integration intervals.

230 For a given initial time t_0 , the integration time $T > 0$ is increased as long as a coherent vortex boundary can be identified. This defines the maximal coherence time $T_{\text{exp}}(t_0)$, i.e., the largest interval over which a vortex persists on $[t_0, t_0 + T]$. Repeating this procedure over a range of initial times yields a function $T_{\text{exp}}(t_0)$ that typically exhibits an approximately wedge-shaped profile, reflecting the progressive loss of material coherence away from an optimal initialization time.

235 In the presence of a finite coherence horizon τ , this wedge is truncated so that $T_{\text{exp}}(t_0) \leq \tau$. The vortex death time is then estimated as $t_{\text{death}} = t_0^{\text{late}} + \tau$, where t_0^{late} denotes the latest initial time for which $T_{\text{exp}}(t_0)$ remains close to τ . The birth time is obtained analogously by applying the same procedure backward in time from t_{death} , yielding $t_{\text{birth}} = t_0^{\text{early}} - \tau$, where t_0^{early} is the earliest initial time for which $|T_{\text{exp}}(t_0)|$ remains close to τ .

240 Equivalently, the procedure defines a set of expectation times $t_{\text{expt}} = t_0 + T_{\text{exp}}(t_0)$, computed in both forward and backward time. The birth and death dates correspond to the earliest and latest such expectation times, respectively, providing a consistent estimate of the vortex life cycle without prescribing a fixed integration interval.



When the inferred lifetime $t_{\text{death}} - t_{\text{birth}}$ is comparable to the coherence horizon τ , the boundary at t_{death} can be viewed as the advected image of the boundary at t_{birth} . In most cases, however, the lifetime exceeds the maximal coherence interval supported by the flow, and the detected structures are therefore better interpreted as quasi-coherent vortices, maintaining material coherence only over finite overlapping time windows.

245 A3 Numerical implementation

We use ERA5 reanalysis winds (Hersbach et al., 2020) on isentropic surfaces, with velocity fields interpolated in space and time to obtain continuous representations suitable for trajectory integration.

Trajectories are computed by integrating $\dot{\mathbf{x}} = \mathbf{u}(\mathbf{x}, t)$ using a fifth-order Runge–Kutta method (Tsitouras scheme) Tsitouras (2011), with the velocity field evaluated at intermediate stages by cubic interpolation in space and time. The flow map gradient
250 is approximated using finite differences based on neighboring trajectories.

The Cauchy–Green tensor is evaluated on a uniform grid of 256×256 points on each isentropic surface, and its eigenvalues and eigenvectors are computed at each grid point. Closed orbits of the line field (A.2) are obtained numerically by integrating the line field starting from selected initial conditions and identifying limit cycles via a Poincaré return map. Because \mathbf{I}_p^\pm defines
255 a line field rather than a globally oriented vector field, its integration requires locally consistent orientation choices along trajectories. This is handled by enforcing continuity of direction during integration. The integration itself is performed using the same Runge–Kutta scheme employed for fluid trajectory computation.

The resulting candidate loops are filtered to retain smooth, non-self-intersecting closed curves, and among nested families the outermost loop is selected as the vortex boundary. All computations are performed using the `CoherentStructures.jl` package, adapted to spherical geometry (Andrade-Canto et al., 2025).

260 *Code availability.* The computational framework used in this study builds on the Julia package `CoherentStructures.jl`, developed by Daniel Karrasch. A working implementation adapted to flows on curved surfaces is available via Gage Bonner at <https://github.com/70Gage70/CoherentLagrangianVortices>.

Data availability. The atmospheric velocity data are obtained from the European Centre for Medium-Range Weather Forecasts (ECMWF) Reanalysis v5 (ERA5), accessible at <https://www.ecmwf.int/en/forecasts/dataset/ecmwf-reanalysis-v5>. These data are publicly available sub-
265 ject to ECMWF terms of use.

Author contributions. FAC and FJBV contributed equally to this work. Both authors designed the study, performed the analysis, and wrote the manuscript.

<https://doi.org/10.5194/egusphere-2026-2375>

Preprint. Discussion started: 27 May 2026

© Author(s) 2026. CC BY 4.0 License.



Competing interests. The authors declare that they have no conflict of interest.

Acknowledgements. The authors thank Gage Bonner for providing the implementation used in this work.

270 *Financial support.* This research received no external funding. No institutional funds were available from ECOSUR (Mexico) or the University of Miami to support publication costs.



References

- Allen, D. R., Fromm, M. D., Kablick III, G. P., and Nedoluha, G. E.: Smoke with Induced Rotation and Lofting (SWIRL) in the stratosphere, *Journal of the Atmospheric Sciences*, 77, 4297–4316, <https://doi.org/10.1175/jas-d-20-0131.1>, 2020.
- 275 Andrade-Canto, F., Karrasch, D., and Beron-Vera, F. J.: Genesis, evolution, and apocalypse of Loop Current rings, *Phys. Fluids*, 32, 116 603, 2020.
- Andrade-Canto, F., Beron-Vera, F. J., and Bonner, G.: Geodesic vortex detection on curved surfaces: Analyzing the 2002 austral stratospheric polar vortex warming event, *Chaos*, 35, 053 140, <https://doi.org/10.1063/5.0256314>, 2025.
- Andrade-Canto, F. and Beron-Vera, F. J.: Do eddies connect the tropical Atlantic Ocean and the Gulf of Mexico?, *Geophysical Research Letters*, 49, e2022GL099 637, <https://doi.org/10.1029/2022gl099637>, 2022.
- 280 Curbelo, J. and Rypina, I. I.: A Three Dimensional Lagrangian Analysis of the Smoke Plume From the 2019/2020 Australian Wildfire Event, *Journal of Geophysical Research: Atmospheres*, 128, <https://doi.org/10.1029/2023jd039773>, 2023.
- de Laat, A. T. J., Stein Zweers, D. C., Boers, R., and Tuinder, O. N. E.: A solar escalator: Observational evidence of the self-lifting of smoke and aerosols by absorption of solar radiation in the February 2009 Australian Black Saturday plume, *Journal of Geophysical Research: Atmospheres*, 117, <https://doi.org/10.1029/2011jd017016>, 2012.
- 285 Fromm, M., Lindsey, D. T., Servranckx, R., Yue, G., Trickl, T., Sica, R., Doucet, P., and Godin-Beekmann, S.: The Untold Story of Pyrocumulonimbus, *Bulletin of the American Meteorological Society*, 91, 1193–1210, <https://doi.org/10.1175/2010bams3004.1>, 2010.
- Haller, G.: Lagrangian Coherent Structures, *Ann. Rev. Fluid Mech.*, 47, 137–162, <https://doi.org/10.1146/annurev-fluid-010313-141322>, 2015.
- 290 Haller, G.: *Transport Barriers and Coherent Structures in Flow Data*, Cambridge University Press, Cambridge, United Kindom, ISBN 9781009225175, <https://doi.org/10.1017/9781009225199>, 2023.
- Haller, G. and Beron-Vera, F. J.: Coherent Lagrangian vortices: The black holes of turbulence, *J. Fluid Mech.*, 731, R4, 2013.
- Haller, G. and Beron-Vera, F. J.: Addendum to ‘Coherent Lagrangian vortices: The black holes of turbulence’, *J. Fluid Mech.*, 755, R3, 2014.
- Haynes, P.: Stratospheric dynamics, *Annu. Rev. Fluid Mech.*, 37, 263–293, 2005.
- 295 Hersbach, H., Bell, B., Berrisford, P., Hirahara, S., Horányi, A., Muñoz-Sabater, J., Nicolas, J., Peubey, C., Radu, R., Schepers, D., Simmons, A., Soci, C., Abdalla, S., Abellan, X., Balsamo, G., Bechtold, P., Biavati, G., Bidlot, J., Bonavita, M., Chiara, G., Dahlgren, P., Dee, D., Diamantakis, M., Dragani, R., Flemming, J., Forbes, R., Fuentes, M., Geer, A., Haimberger, L., Healy, S., Hogan, R. J., Hólm, E., Janisková, M., Keeley, S., Laloyaux, P., Lopez, P., Lupu, C., Radnoti, G., Rosnay, P., Rozum, I., Vamborg, F., Villaume, S., and Thépaut, J.: The ERA5 global reanalysis, *Quarterly Journal of the Royal Meteorological Society*, 146, 1999–2049, 2020.
- 300 Holton, J. R.: *An introduction to dynamic meteorology*, Academic, second edn., 1979.
- Kablick, G. P., Allen, D. R., Fromm, M. D., and Nedoluha, G. E.: Australian PyroCb Smoke Generates Synoptic-Scale Stratospheric Anticyclones, *Geophysical Research Letters*, 47, <https://doi.org/10.1029/2020gl088101>, 2020.
- Karrasch, D., Huhn, F., and Haller, G.: Automated detection of coherent Lagrangian vortices in two-dimensional unsteady flows, *Proc. Royal Soc. A*, 471, 20140 639, 2014.
- 305 Khaykin, S., Legras, B., Bucci, S., Sellitto, P., Isaksen, L., Tencé, F., Bekki, S., Bourassa, A., Rieger, L., Zawada, D., Jumelet, J., and Godin-Beekmann, S.: The 2019/20 Australian wildfires generated a persistent smoke-charged vortex rising up to 35-km altitude, *Communications Earth & Environment*, 1, <https://doi.org/10.1038/s43247-020-00022-5>, 2020.



- Lestrelin, H., Legras, B., Podglajen, A., and Salihoglu, M.: Smoke-charged vortices in the stratosphere generated by wildfires and their behaviour in both hemispheres: comparing Australia 2020 to Canada 2017, *Atmospheric Chemistry and Physics*, 21, 7113–7134, <https://doi.org/10.5194/acp-21-7113-2021>, 2021.
- McIntyre, M.: DYNAMICAL METEOROLOGY I Balanced Flow, p. 298–303, Elsevier, ISBN 9780123822253, <https://doi.org/10.1016/b978-0-12-382225-3.00484-9>, 2015.
- Peterson, D. A., Campbell, J. R., Hyer, E. J., Fromm, M. D., Kablick, G. P., Cossuth, J. H., and DeLand, M. T.: Wildfire-driven thunderstorms cause a volcano-like stratospheric injection of smoke, *npj Climate and Atmospheric Science*, 1, <https://doi.org/10.1038/s41612-018-0039-3>, 2018.
- Tsitouras, C.: Runge–Kutta pairs of order 5(4) satisfying only the first column simplifying assumption, *Computers & Mathematics with Applications*, 62, 770–775, <https://doi.org/10.1016/j.camwa.2011.06.002>, 2011.
- Yu, P., Toon, O. B., Bardeen, C. G., Zhu, Y., Rosenlof, K. H., Portmann, R. W., Thornberry, T. D., Gao, R.-S., Davis, S. M., Wolf, E. T., de Gouw, J., Peterson, D. A., Fromm, M. D., and Robock, A.: Black carbon lofts wildfire smoke high into the stratosphere to form a persistent plume, *Science*, 365, 587–590, <https://doi.org/10.1126/science.aax1748>, 2019.

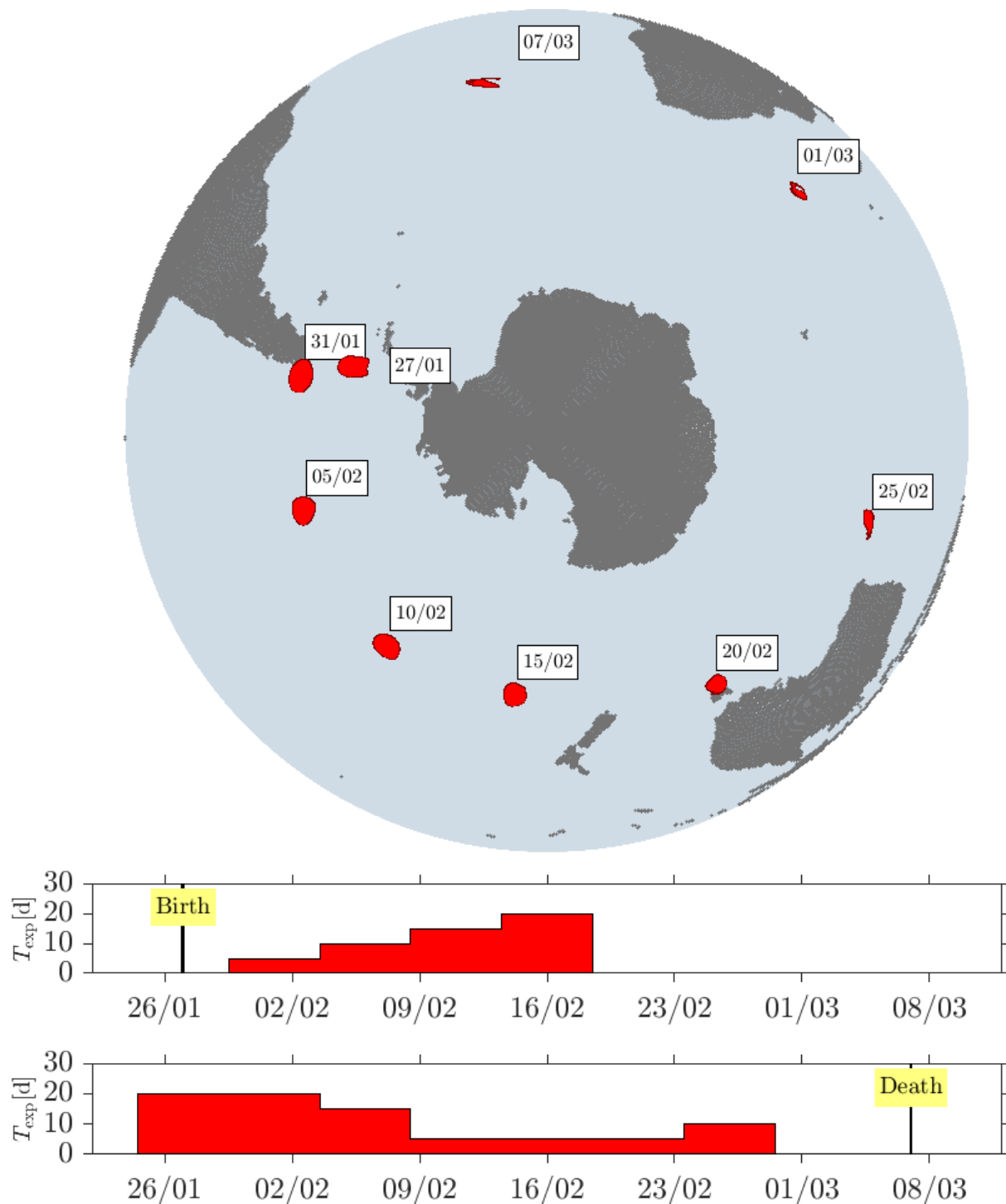


Figure 1. Life-cycle identification at 690 K. Top: spatial evolution of the vortex boundary. Middle: backward-time coherence-time function $T_{exp}(t_0)$; the marked time indicates vortex birth. Bottom: forward-time coherence-time function $T_{exp}(t_0)$; the marked time indicates vortex death.

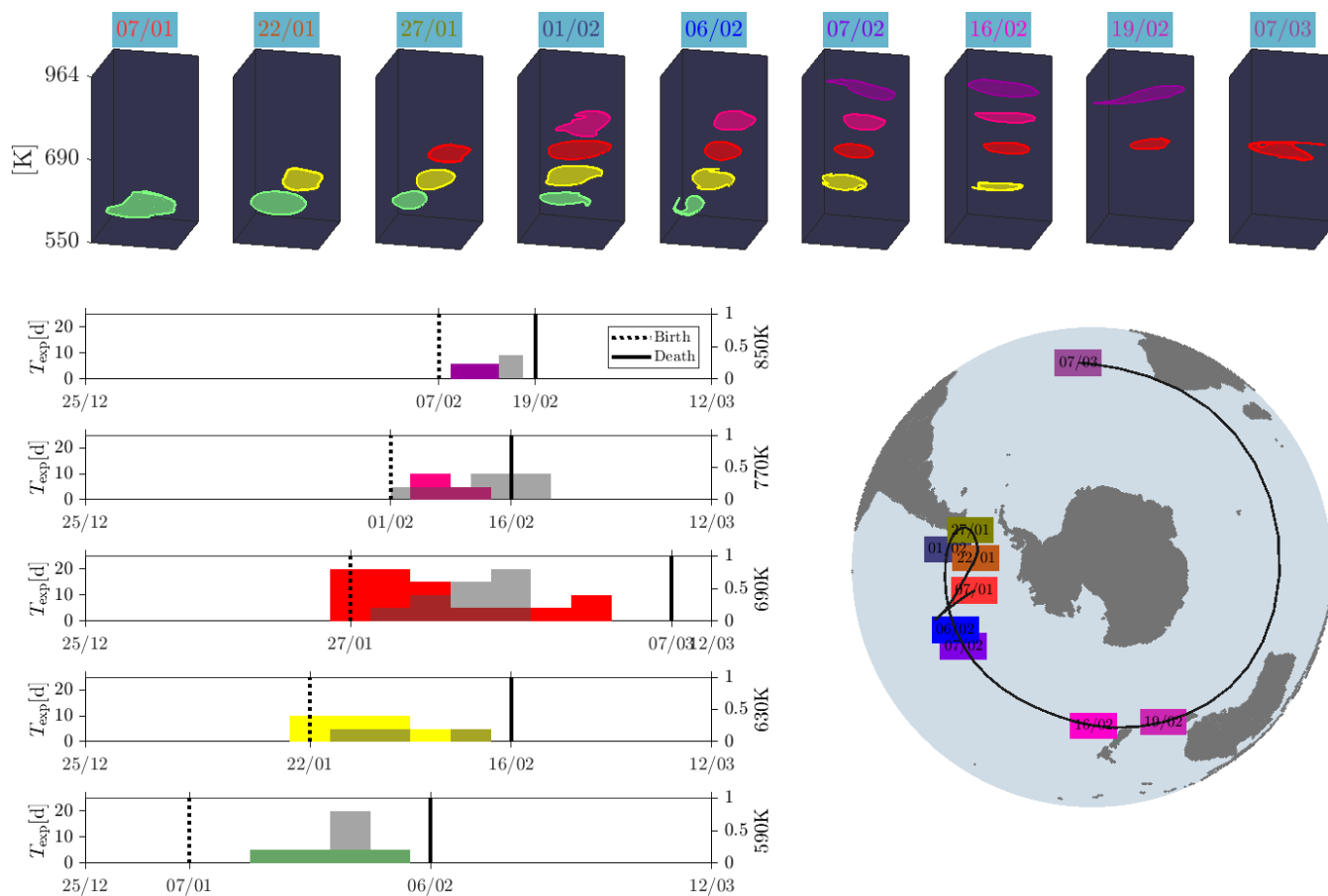


Figure 2. Life-cycle diagnostics, vertical structure, and trajectory of Koobor. Left: coherence-time function $T_{exp}(t_0)$ at each isentropic level (forward in color, backward in gray). Top: evolution of vortex boundaries at each level, shown only during coherent intervals. Bottom right: horizontal trajectory of the vortex.

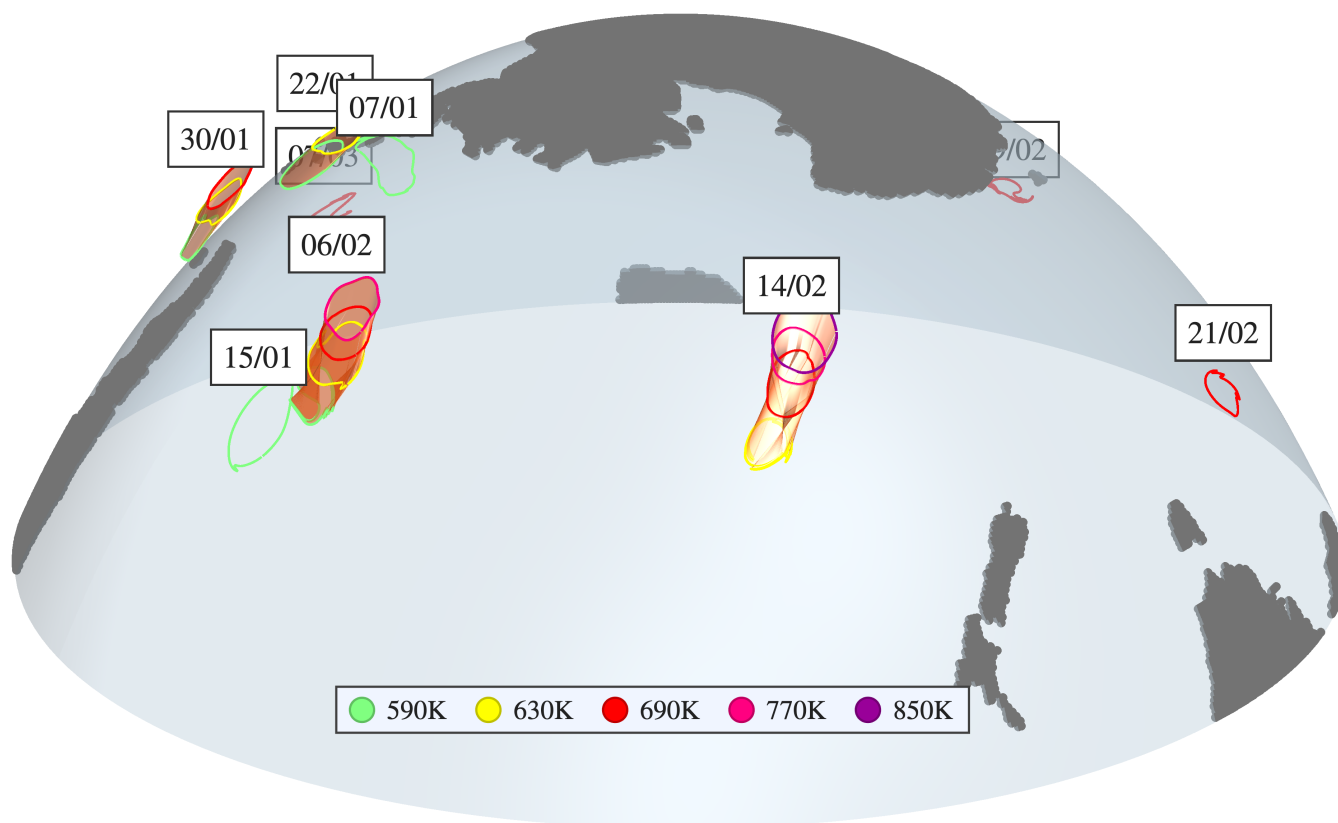


Figure 3. Global synthesis of *Koobor* evolution. Colored curves denote vortex boundaries at individual isentropic levels, shown only during coherent intervals. For selected dates, translucent surfaces ("tubes") connect these boundaries across levels, visualizing the instantaneous vertical organization of the vortex.